Theranostics

DOI: 10.1002/ange.201308986

Biodegradable Gold Nanovesicles with an Ultrastrong Plasmonic Coupling Effect for Photoacoustic Imaging and Photothermal Therapy**

Peng Huang, Jing Lin, Wanwan Li, Pengfei Rong, Zhe Wang, Shouju Wang, Xiaoping Wang, Xiaolian Sun, Maria Aronova, Gang Niu, Richard D. Leapman, Zhihong Nie, and Xiaoyuan Chen**

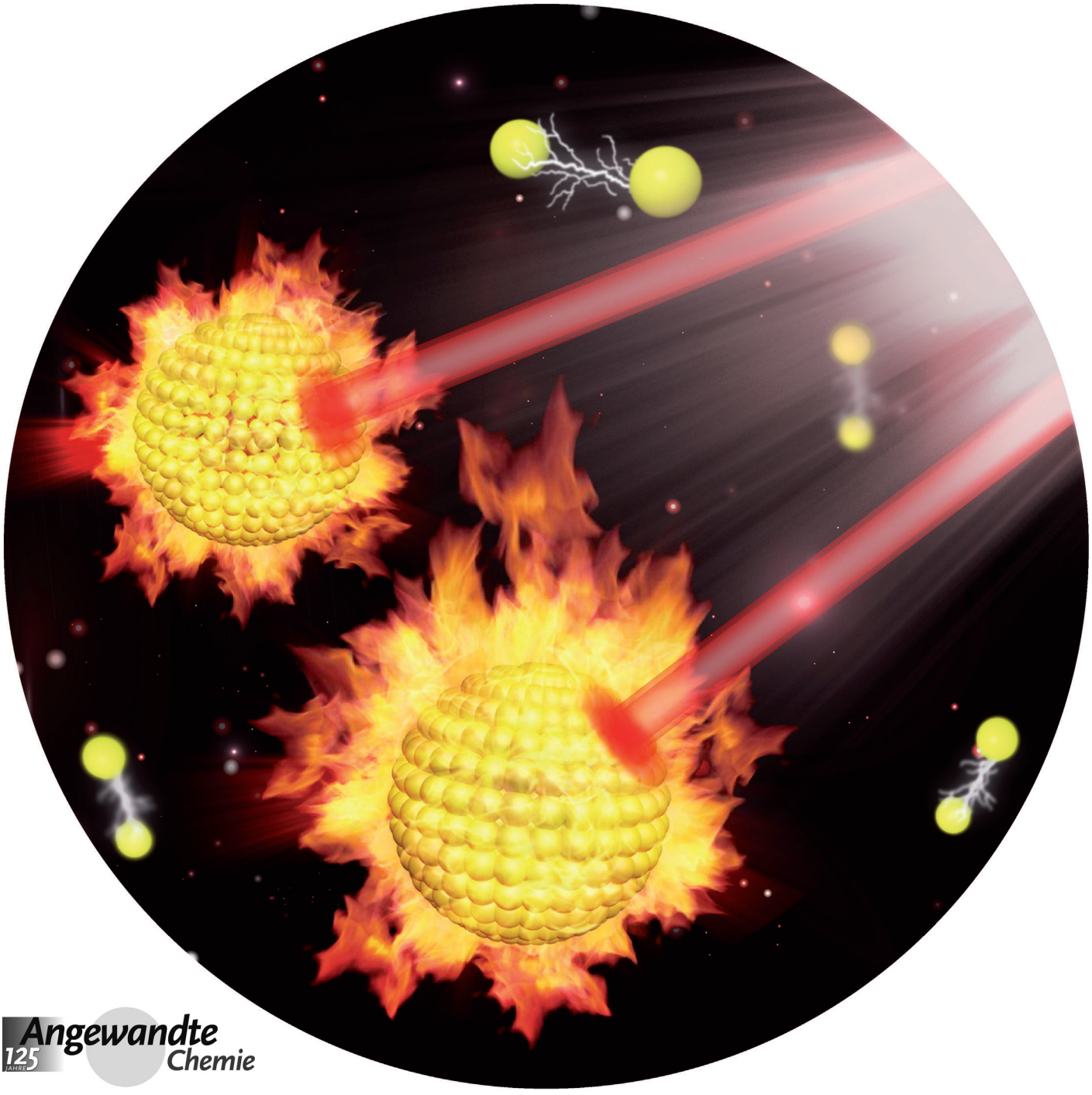

Abstract: *The hierarchical assembly of gold nanoparticles (GNPs) allows the localized surface plasmon resonance peaks to be engineered to the near-infrared (NIR) region for enhanced photothermal therapy (PTT). Herein we report a novel theranostic platform based on biodegradable plasmonic gold nanovesicles for photoacoustic (PA) imaging and PTT. The disulfide bond at the terminus of a PEG-b-PCL block-copolymer graft enables dense packing of GNPs during the assembly process and induces ultrastrong plasmonic coupling between adjacent GNPs. The strong NIR absorption induced by plasmon coupling and very high photothermal conversion efficiency ($\eta = 37\,\%$) enable simultaneous thermal/PA imaging and enhanced PTT efficacy with improved clearance of the dissociated particles after the completion of PTT. The assembly of various nanocrystals with tailored optical, magnetic, and electronic properties into vesicle architectures opens new possibilities for the construction of multifunctional biodegradable platforms for biomedical applications.*

Photothermal therapy (PTT), owing to its specific spatial/temporal selectivity and minimal invasiveness, has been increasingly recognized in cancer treatment.[1] Various inorganic/organic nanomaterials have been used as photothermal conversion agents (PTCAs).[2] However, most of these agents have not yet been approved for clinical application, most likely as a result of their poor pharmacokinetics and potential long-term toxicity.[3] An ideal PTCA is expected to have the following features: 1) strong absorption in the near-infrared (NIR) region, in which skin, tissues, and hemoglobin show minimal absorption;[2f,3] 2) high photothermal conversion efficiency and good thermal conductivity through fast absorption of optical energy, instant conversion into heat, and rapid transmission to the surrounding tissues/cells; 3) good biocompatibility and biodegradability,[2b,3] with little to no toxicity and ready clearance from the body; 4) convenient and real-time visualization of in vivo PTCA delivery and distribution, and monitoring of treatment efficacy.[4]

Plasmonic PTCAs, particularly gold-based nanostructures that can absorb and transfer optical energy into heat by the Landau damping effect with high efficiency, have received great interest in the field of PTT.[5] Early clinical studies with Auroshell particles (gold nanoshells (GNSs) coated with polyethylene glycol 500 and with a size of 150 nm) have shown some promise in cancer PTT treatment; however, the large nanoparticles tend to show slow excretion from the body.[6] In the case of gold nanorods (GNRs), the toxicity derived from the cetyltrimethylammonium bromide (CTAB) surfactant used during their synthesis severely limits their biomedical application.[1b,5c] As for gold nanoparticles (GNPs), their absorption is not optimal for PTT:[5b,7] the localized surface plasmon resonance (LSPR) peaks occur at 520 nm for 10 nm GNPs and at 580 nm for 100 nm GNPs. The hierarchical assembly of GNPs allows one to engineer the LSPR peaks to the NIR region for enhanced PTT with improved clearance after the dissociation of assemblies. Recently, we demonstrated that vesicular/clustered gold vesicle (GV) assemblies composed of poly(ethylene glycol)-*b*-polystyrene (PEG-*b*-PS)-tethered GNPs show LSPR absorbance in the range of 650–800 nm owing to plasmon coupling between adjacent GNPs.[8] However, the assemblies based on the PEG-*b*-PS polymer were nonbiodegradable and showed suboptimal photothermal conversion efficiency. It is thus highly desirable to develop novel biodegradable polymer/GNPs assemblies with high photothermal conversion efficiency for PTT to enable the breakdown of vesicles into smaller discrete GNPs after the completion of PTT, followed by rapid clearance of the dissociated particles.

Herein we report a novel design of biodegradable gold nanovesicles (BGVs) composed of poly(ethylene glycol)-*b*-poly(ε-caprolactone) (PEG-*b*-PCL)-tethered GNPs with an ultrastrong plasmonic coupling effect for photoacoustic (PA) imaging and PTT (Figure 1; see also Scheme S1 in the Supporting Information). The PEG-*b*-PCL polymer with a disulfide bond (S–S) at the terminus was grafted onto the surface of GNPs, and then the formation of BGVs in a THF/water system was guided by dialysis. Reduction of the distance (d) between adjacent GNPs during the assembly process by the PEG-*b*-PCL polymer graft induces an ultrastrong plasmonic coupling effect. The formation of abundant inter-nanoparticle junctions can be used to tune the LSPR peak of the original GNPs from the visible to the NIR region. The BGVs with strong absorption in the NIR region showed an excellent PA response and enhanced photothermal conversion efficiency upon laser irradiation.

GNPs with a diameter of (26.2 ± 1.45) nm were prepared by the use of citrate to reduce chloroauric acid in the aqueous phase. Plasmonic BGVs were prepared by assembling GNPs tethered with the S–S-terminated amphiphilic block copolymer (BCP), PEO_{45}-*b*-PCL_{270} ($M_n = 24.4\ kg\,mol^{-1}$, polydispers-

[*] Dr. P. Huang,[+] Dr. W. Li, P. Rong, Dr. Z. Wang, Dr. S. Wang, X. Wang, Dr. X. Sun, Dr. G. Niu, Prof. X. Chen
Laboratory of Molecular Imaging and Nanomedicine (LOMIN)
National Institute of Biomedical Imaging and Bioengineering (NIBIB), National Institutes of Health (USA)
E-mail: shawn.chen@nih.gov

Dr. J. Lin,[+] Prof. Z. Nie
Department of Chemistry and Biochemistry, University of Maryland
College Park, MD 20742 (USA)
E-mail: znie@umd.edu

Dr. M. Aronova, Prof. R. D. Leapman
Laboratory of Cellular Imaging and Macromolecular Biophysics
NIBIB, National Institutes of Health (USA)

Dr. Z. Wang
Center for Molecular Imaging and Translational Medicine
School of Public Health, Xiamen University
Xiamen, 361005 (China)

[+] These authors contributed equally.

[**] This research was supported by the startup funds of the University of Maryland, the Intramural Research Program (IRP) of the NIBIB, the NIH, the National Key Basic Research Program (973 Project; 2010CB933901, 2013CB733802, 2014CB744503), the National Science Foundation of China (81272987, 31170961, 51102258, 81371596), and a Chinese Academy of Sciences Professorship for Senior International Scientists (2011T2J06).

Supporting information for this article is available on the WWW under http://dx.doi.org/10.1002/anie.201308986.

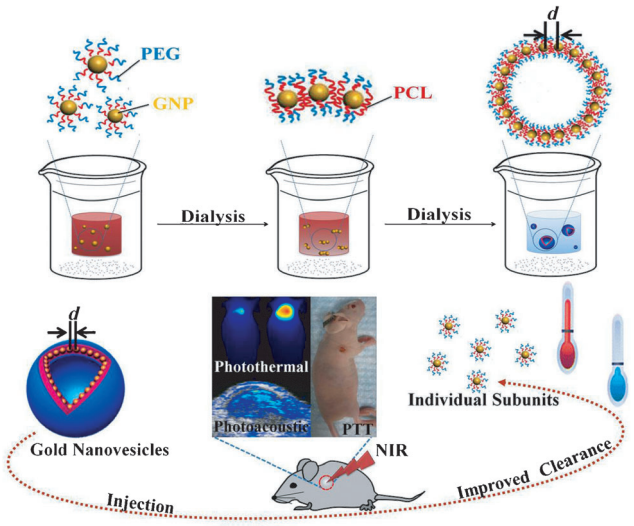

Figure 1. Self-assembly of biodegradable gold vesicles (BGVs) composed of poly(ethylene glycol)-*b*-poly(ε-caprolactone) (PEG-*b*-PCL)-tethered GNPs through the dot–line–plane–vesicle mode during the dialysis process. BGVs with an ultrastrong plasmonic coupling effect are superior photoacoustic (PA) imaging and photothermal therapy (PTT) agents with improved clearance after the dissociation of the assemblies. The PA signal and PTT efficiency of BGVs are increased as the distance (*d*) between adjacent GNPs decreases.

ity index (PDI) = 1.22), followed by dialysis in water of a concentrated solution of the GNPs in THF. The self-assembly of PEG-*b*-PS-tethered GNPs into GVs was carried out according to our previously reported method.[9] The self-assembly process is governed by the balance of attractive forces, namely, hydrophilic/hydrophobic interactions of amphiphilic BCPs. The representative SEM and TEM images in Figure 2a–c show the well-defined vesicular assemblies of GNPs. The BGVs are composed of a single layer of seamlessly packed GNPs in the vesicular membranes. The hollow interior of the assemblies was clearly confirmed by the morphology of broken BGVs (inset of Figure 2a). As shown in Figure 2c, owing to the presence of rigid benzene rings in the polystyrene part of PEG-*b*-PS, the GNPs are more separated from each other in the GVs than in the BGVs with the more flexible PEG-*b*-PCL tether.

To better understand how the BGVs are formed, we varied the concentration of the solution of GNPs in THF (12.5, 37.5, 50, 100, 150, and 250 μg mL^{-1}) during the dialysis in water. BGVs were produced when the GNP concentration was more than 50 μg mL^{-1} (see Figure S3). At lower GNP concentrations (< 50 μg mL^{-1}), gold clusters were formed instead. When the GNP concentration was over 100 μg mL^{-1}, almost all of the GNPs were assembled into BGVs. The size of the BGVs was dependent on the concentration of GNPs (see Figure S4). At a GNP concentration of 100 and 150 μg mL^{-1}, the BGVs exhibited a relatively narrow size distribution of (192.6 ± 11.8) and (207.3 ± 15.7) nm, respectively. When the GNP concentration reached 250 μg mL^{-1}, huge submicron-sized BGVs were formed. The assembly of GNPs led to short interparticle distances; thus, a redshift in the extinction spectra was observed owing to a strong plasmonic coupling effect between adjacent GNPs.[10] This process is accompanied by a color change of the solution from red to dark blue (see Figure S5). For the GVs composed of PEG-*b*-PS-tethered GNPs, the LSPR peak shifted from 518 to 630 nm (Figure 2d; see also Figure S5). For the BGVs composed of PEG-*b*-PCL-tethered GNPs, the LSPR peaks were broadened, and the major peak moved to 808 (BGV1), 902 (BGV2), and 1008 nm (BGV3) as the GNP concentration increased.

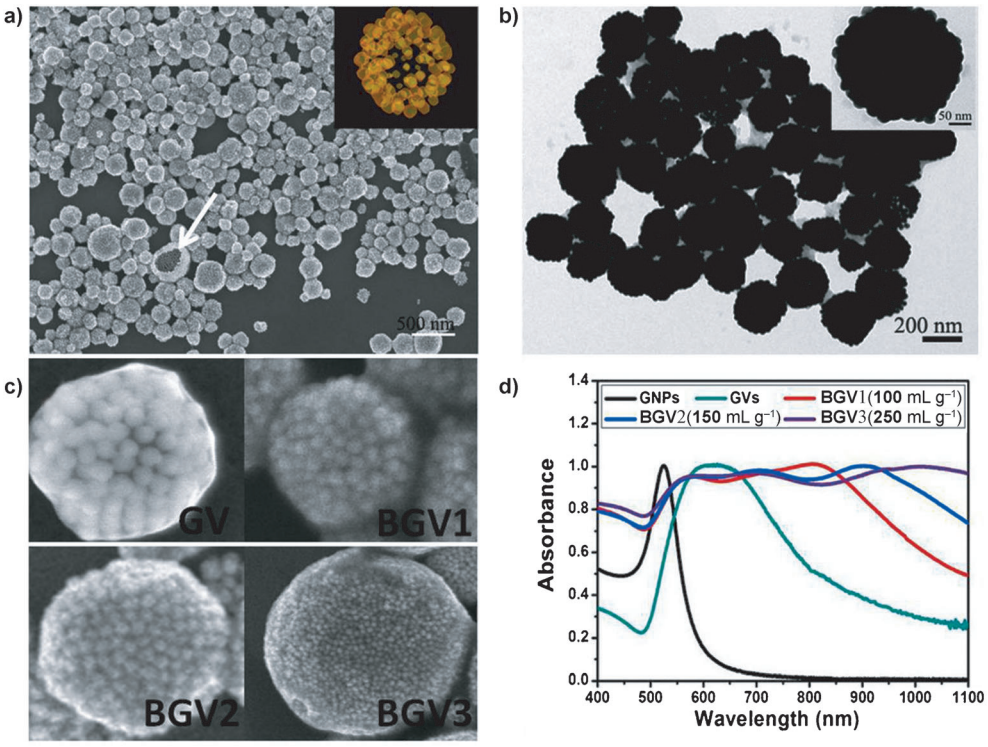

Figure 2. Plasmonic BGVs self-assembled from GNPs ((26.2 ± 1.45) nm). a) SEM (inset: 3D electron-density mapping of a broken BGV) and b) TEM images (inset: individual BGV; scale bar: 50 nm). c) SEM images of GV (top left), BGV1 (top right), BGV2 (bottom left), and BGV3 particles (bottom right). d) UV/Vis/NIR spectra of GNPs, PEG-*b*-PS-tethered gold vesicles (GVs), and block-copolymer-tethered biodegradable gold vesicles produced by the dialysis of solutions of GNPs (100, 150, and 250 μg mL^{-1}) in THF. The LSPR peaks of the BGVs can be tuned by varying the GNP concentration.

The strong NIR absorption of BGV1 at around 800 nm motivated us to investigate the potential of these vesicles in the PTT of cancer with an 808 nm laser. Different gold nanomaterials were dispersed in water and then irradiated with a suitable laser (Figure 3a). No obvious temperature change was observed in the control of pure water. Upon laser illumination for 5 min (laser power: 1 W cm^{-2}), the GNPs, GNRs, GVs, and BGVs raised the temperature by 8.0, 24.0, 23.6, and 40.7 °C, respectively. The photothermal effect of the BGVs increased monotonically with particle concentration and radiant energy (see Figure S6).

Next, we measured the photothermal conversion efficiency (η) of the BGVs. The η value was calculated according to the energy balance of the system as follows:[2c,h,4c,11]

$$\eta = (h S \Delta T_{max} - Q_s)/I\,(1-10^{-A808}) \quad (1)$$

$$\tau_s = m_D C_D/hS \quad (2)$$

in which h is the heat-transfer coefficient, S is the surface area of the container, ΔT_{max} is the temperature change of the BGV solution at the maximum steady-state temperature, I is the laser power, $A808$ is the absorbance of the BGVs at 808 nm, and Q_s is the heat associated with light absorption by the solvent. The variable τ_s is the sample-system time constant, and m_D and C_D are the mass (0.2 g) and heat capacity (4.2 J g^{-1}) of the deionized water used as the solvent. According to Equations (1) and (2), the η value of the BGVs was determined to be 37% (see Figure S7). The η value of the BGVs is markedly higher than the corresponding values for GVs (18%), GNRs (22%), and GNSs (13%; Figure 3b),[11] thus suggesting high efficiency of the BGVs in the conversion of the 808 nm laser energy into heat owing to the presence of an ultrastrong plasmonic coupling effect.

We further investigated the biodegradability of the BGVs by subjecting them to different conditions. We found that the assembled BGVs gradually collapsed as the temperature of the solution was increased (Figure 3c). When the temperature of the system was over 70 °C, the majority of the BGVs were dissociated after 10 min, since the melting point of PCL is about 60 °C.[12] We found that small holes appeared in the membranes of the BGVs at a time of 1 week (see Figure S8). Afterwards, defects between adjacent GNPs became more evident, and major fragments were observed to fall off the vesicles at 4 weeks. Finally, all BGVs had completely collapsed at 8 weeks. On the basis of these results, we predict that the in vivo dissociation of the BGVs should be shorter, owing to the complex conditions in the body, including abundant enzymes. These results suggest that the BGVs can be gradually degraded into discrete GNPs in both a temperature-and time-dependent manner.

The NIR-laser-triggered cell-killing effect of the BGVs was assessed by a standard 3-(4,5-dimethylthiazol-2-yl)-2,5-diphenyltetrazolium bromide (MTT) assay[13] (see Figure S9a). Cell viability was normalized to a control group without any treatment. Without laser irradiation, the BGVs exhibited negligible toxicity to MDA-MB-435 cells. Upon laser irradiation, the BGVs induced concentration- and laser-dose-dependent cytotoxicity to MDA-MB-435 cells. The cell viability of irradiated groups gradually decreased as the BGV concentration increased. Upon the extension of the treatment to 10 min, almost all cells were killed at all tested concentrations. To further identify cell viability, we costained the cells with Calcein AM and ethidium homodimer-1 to differentiate live (green) and dead (red) cells, respectively (see Figure S9b–d). In the control group, all cells displayed green fluorescence, which suggests that laser irradiation alone is not able to kill tumor cells. In the BGV group, all cells were killed, as indicated by the intense homogeneous red fluorescence. Meanwhile, we found that all cells within the laser spot were killed,

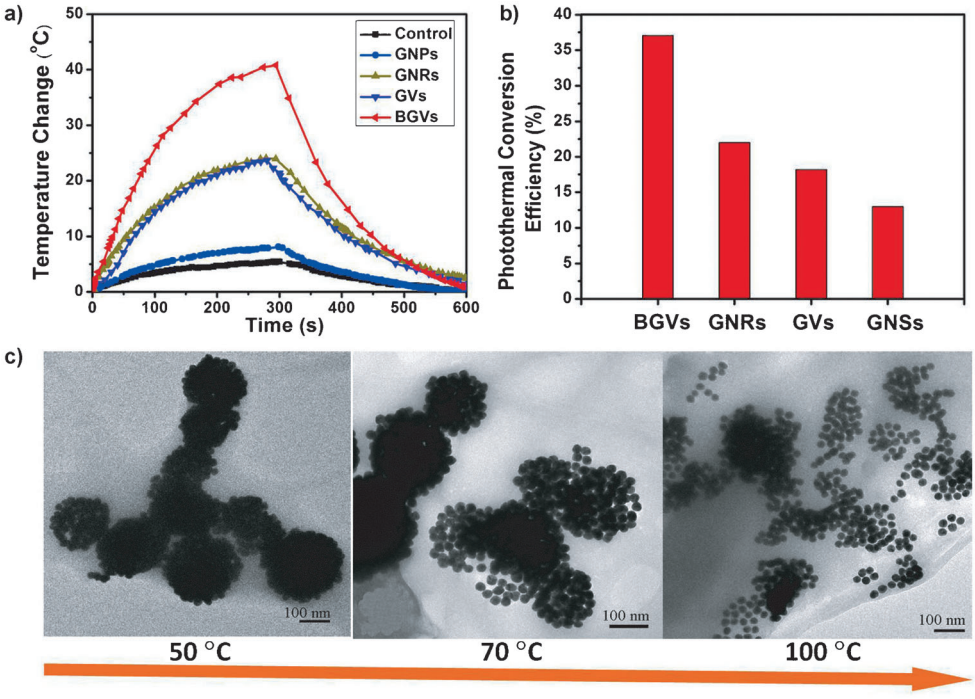

Figure 3. a) Temperature elevation of aqueous solutions of GNPs (at the same Au concentration as that of the BGVs, λ_{ex} = 808 nm), GNRs (OD@808 nm = 1, λ_{ex} = 808 nm), GVs (OD@671 nm = 1, λ_{ex} = 671 nm), and BGVs (OD@808 nm = 1, λ_{ex} = 808 nm) exposed to laser irradiation (1 W cm^{-2}) as a function of irradiation time. Irradiation was continued for 5 min, and then the laser was turned off. Pure water was used as a negative control. b) Photothermal conversion efficiencies of BGVs, GVs, GNRs, and GNSs. c) TEM images of BGVs after treatment at different temperatures for 10 min.

whereas cells without irradiation (outside the region of the laser spot) displayed green fluorescence. This result indicates that PTT treatment with the BGVs is highly selective and localized.

Encouraged by the in vitro PTT effect of the BGVs, we then investigated the feasibility of using the BGVs for in vivo PT/PA imaging and PTT in a MDA-MB-435 tumor-xenograft model. When the tumors in mice reached a size of about 60 mm^3, the mice were treated by intratumoral injection with BGVs (400 $\mu g\,mL^{-1}$, 50 μL). Thermal imaging with an infrared thermal camera was used to monitor the efficacy of treatment in vivo (Figure 4a,b). Under 808 nm laser irradiation at a power of both 0.5 and 1 $W\,cm^{-2}$, the local tumor temperature rapidly increased by over 18° within 5 min; the resulting temperature was high enough to kill tumor cells in vivo. No significant temperature increase was observed in other body parts of the mice (see Figure S10). Upon intratumoral administration of the same amount of GNRs, followed by 808 nm laser irradiation at 1 $W\,cm^{-2}$, the local temperature change was about 10 °C within 5 min. Upon intratumoral administration of the same amount of GVs and 671 nm laser irradiation at 2 $W\,cm^{-2}$, the local temperature change was about 8 °C within 5 min.

PA imaging was employed to evaluate the PA properties of the BGVs and guide the intratumoral injection (see Video S1 in the Supporting Information). When the BGV concentration was increased, a linear correlation between the PA signal intensity and the BGV concentration was observed ($R^2 = 0.994$), as described by the following typical equation: $Y = 0.16 + 46.50X$ (Figure 4c). As compared with GNRs (see Figure S11), the BGVs showed a much stronger PA signal at the same value of optical density (OD) at 808 nm. Intense PA signals were observed in the tumor region injected with the BGVs (Figure 4d; see also Figure S12). As shown in Figure 4e, the average tumor PA intensity of the BGVs was approximately 10-fold stronger than that observed before the

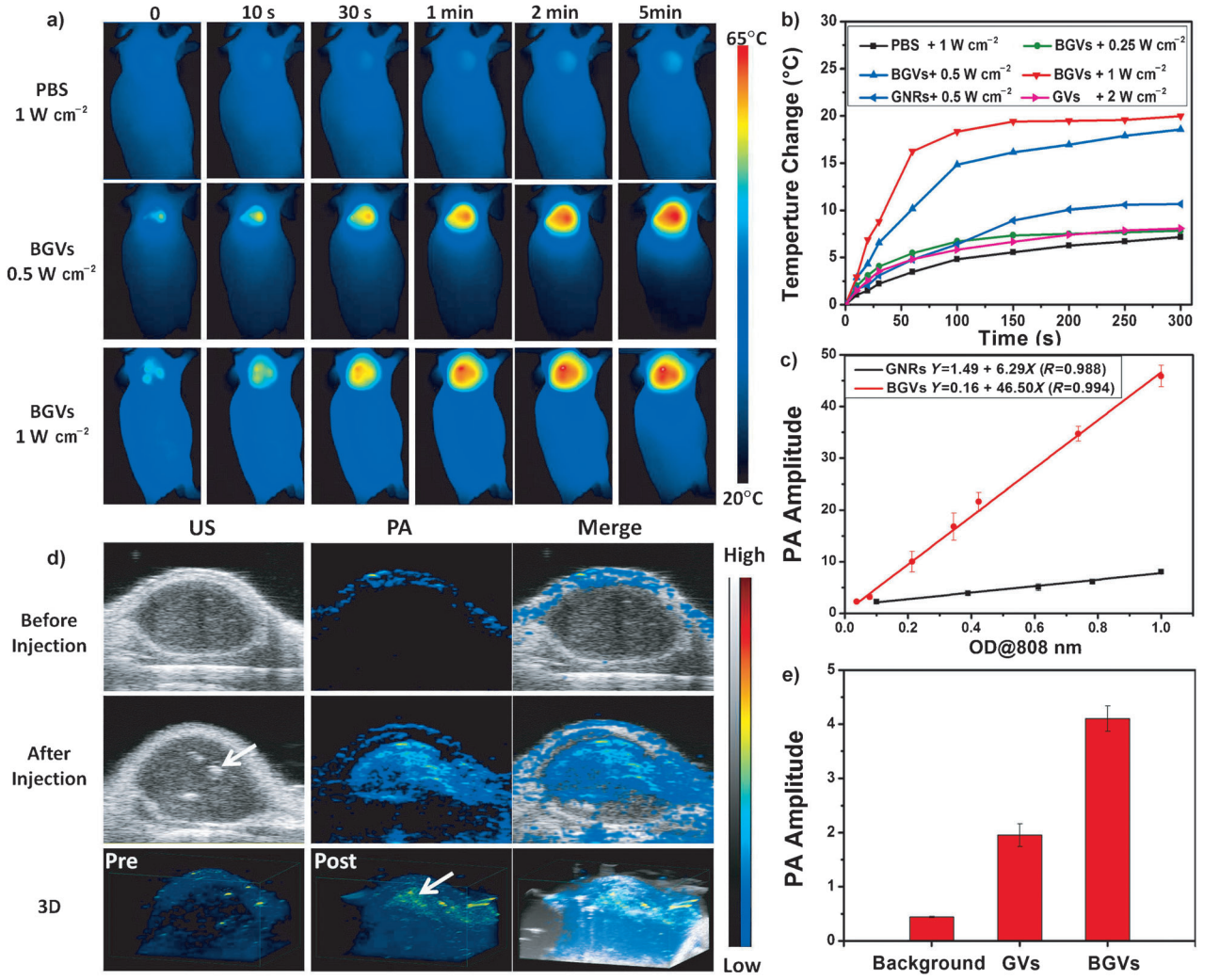

Figure 4. a) Thermal images of MDA-MB-435 tumor-bearing mice exposed to an 808 nm laser for 5 min after the injection of phosphate-buffered saline (PBS) or BGVs. b) Heat curves of tumors upon laser irradiation as a function of irradiation time. c) PA signals of BGVs and GNRs as a function of optical density. d) In vivo 2D ultrasonic (US) and photoacoustic (PA) images and 3D PA images of tumor tissues before and after the injection of BGVs. Arrows indicate the location of BGVs. e) PA intensities of tumor tissues following the intratumoral administration of the same amount of GVs or BGVs.

injection of the BGVs and approximately twice as strong as that observed upon the injection of GVs.

Finally, the BGV-induced PTT effect in vivo was studied. Since their size is over 200 nm, the BGVs are efficient in activating the human complement system and are hence cleared rapidly from the blood circulation and predominantly taken up by the reticuloendothelial system (RES), including the liver (Kupffer cells) and the spleen (marginal zone and red pulp) macrophages.[14] Therefore, the preferred route of BGV administration is intratumoral injection, which is the most efficient way of delivering PTCAs in PTT.[15] Seven groups of MDA-MB-435 tumor-bearing mice with 5–7 mice per group were used in our experiment (Figure 5a). In the treatment groups ($n = 7$ per group), mice were intratumorally injected with BGVs (400 $\mu g\,mL^{-1}$, 50 μL) and then irradiated with a 808 nm laser at a power density of 0.5 or 1 $W\,cm^{-2}$ for 5 min. Other control groups of mice (5 mice per group) included untreated mice, mice administered with BGVs but without laser irradiation, mice subjected to laser irradiation only, mice administered with GNRs and subjected to 808 nm laser irradiation (0.5 $W\,cm^{-2}$), and mice administered with GVs and subjected to 671 nm laser irradiation (2 $W\,cm^{-2}$). Groups administered with GNRs, GVs, and BGVs and subjected to laser irradiation showed a remarkable delay in tumor growth or tumor regression as compared with the control groups after 2 weeks (GNR versus control, $P < 0.001$; GV versus control, $P < 0.001$; BGV versus control, $P < 0.0001$). In the groups administered with BGVs and irradiated with a laser (both at 0.5 and 1 $W\,cm^{-2}$), all the tumors were effectively ablated; black scars were left at the original tumor sites and no reoccurrence was observed (Figure 5a,b). In contrast, the tumors in the control groups all grew at a similar speed (Figure 5a). Notably, the BGV group subjected to a low dose of laser irradiation (0.5 $W\,cm^{-2}$ for 5 min) exhibited significantly higher therapeutic efficacy as compared with the GNR/laser and GV/laser groups on day 14 (BGV versus GV, $P < 0.0001$; BGV versus GNR, $P < 0.0001$). Whereas the mice in the control groups showed average life spans of 14–20 days after treatment started, mice in the BGV-treated groups were tumor-free and survived over 30 days without a single death or tumor reoccurrence; mice in the GNR/laser group showed only a slight delay of tumor growth, and all surviving animals at day 24 had to be sacrificed because of the extensive tumor burden (Figure 5c). Hematoxylin and eosin staining of tumor slices was also carried out for tumors collected immediately after laser irradiation (Figure 5e). We found significant cancer-cell damage in the tumor of the BGV/laser group, but not in the other three control groups. We also investigated the biodistribution of the BGVs after intratumoral injection. Figure 5d shows that BGVs leaked into the circulation and accumulated prominently in the RES, including the liver and spleen, on day 2. BGVs were cleared from the RES on day 8. In the group treated with BGVs only (without laser irradiation), the BGVs always stayed in the tumor tissue (data not shown). These results indicate that BGVs have excellent theranostic capability for PT/PA imaging and PTT of tumors with reasonable clearance most likely as a result of the dissociation of assemblies after laser irradiation and under the physiological conditions over time.

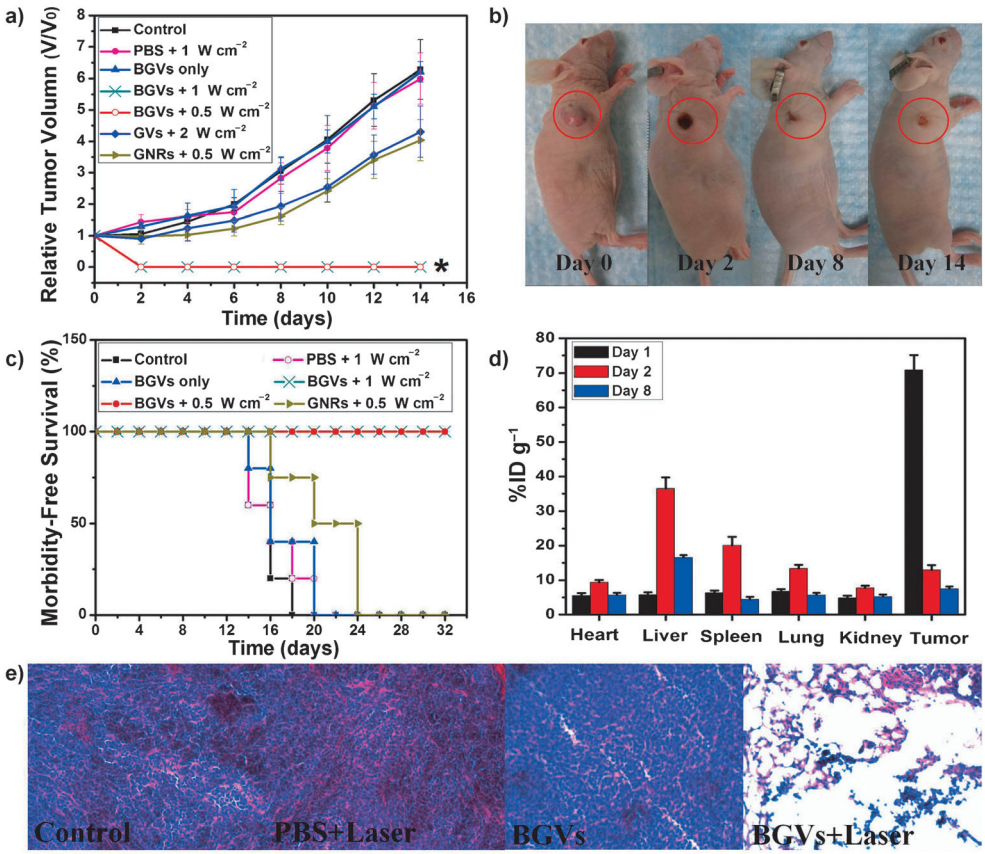

Figure 5. a) Tumor growth curves of different groups of MDA-MB-435 tumor-bearing mice after treatment. Tumor volumes were normalized to their initial sizes. Error bars represent the standard deviation of 5–7 mice per group. Asterisk indicates $P < 0.01$. b) Photographs of MDA-MB-435 tumor-bearing mice at different days after BGV treatment. c) Survival curves of tumor-bearing mice after various treatments. BGV-injected mice after PTT treatment showed 100% survival over 30 days. d) Pharmacokinetics of BGVs after the intratumoral injection of BGVs (400 $\mu g\,mL^{-1}$, 50 μL), as deduced by inductively coupled plasma mass spectrometric analysis of Au in different organs at 1, 2, and 8 days postinjection ($n = 3$ per group). $\%ID\,g^{-1}$ = percentage of the injected dose per gram of tissue. e) Hematoxylin and eosin staining of tumor sections collected from different groups of mice after laser irradiation.

In summary, we have developed a novel theranostic platform based on biodegradable plasmonic gold vesicles for cancer imaging and treatment. The PEG-*b*-PCL BCP graft with a disulfide bond at its terminus allows dense packing of GNPs with specific interparticle orientations during the assembly process and induces an ultrastrong plasmonic coupling effect between adjacent GNPs. The strong NIR absorption induced by plasmon coupling enables thermal/PA imaging and PTT with high efficacy. The BGVs we developed have the following features: 1) high photothermal conversion efficiency ($\eta = 37\,\%$); 2) dissociation into discrete gold nanoparticles at elevated temperatures; 3) simultaneous thermal/PA imaging and enhanced PTT efficacy; 4) improved clearance of the dissociated particles after the completion of PTT. Furthermore, the multifunctional BGVs show high solubility and stability in aqueous media and good biocompatibility, thus facilitating their biomedical application.

Received: October 15, 2013
Revised: November 11, 2013
Published online: December 6, 2013

Keywords: biodegradable block copolymers · gold nanovesicles · photoacoustic imaging · photothermal therapy · plasmonic coupling

[1] a) S. Wang, P. Huang, L. Nie, R. Xing, D. Liu, Z. Wang, J. Lin, S. Chen, G. Niu, G. Lu, X. Chen, *Adv. Mater.* **2013**, *25*, 3055 – 3061; b) P. Huang, L. Bao, C. Zhang, J. Lin, T. Luo, D. Yang, M. He, Z. Li, G. Gao, B. Gao, *Biomaterials* **2011**, *32*, 9796 – 9809; c) J. F. Lovell, C. S. Jin, E. Huynh, H. Jin, C. Kim, J. L. Rubinstein, W. C. W. Chan, W. Cao, L. V. Wang, G. Zheng, *Nat. Mater.* **2011**, *10*, 324 – 332; d) P. Huang, J. Lin, X. Wang, Z. Wang, C. Zhang, M. He, K. Wang, F. Chen, Z. Li, G. Shen, D. Cui, X. Chen, *Adv. Mater.* **2012**, *24*, 5104 – 5110.

[2] a) Q. Tian, M. Tang, Y. Sun, R. Zou, Z. Chen, M. Zhu, S. Yang, J. Wang, J. Wang, J. Hu, *Adv. Mater.* **2011**, *23*, 3542 – 3547; b) Z. Zha, X. Yue, Q. Ren, Z. Dai, *Adv. Mater.* **2012**, *24*, 777 – 782; c) Q. Tian, F. Jiang, R. Zou, Q. Liu, Z. Chen, M. Zhu, S. Yang, J. Wang, J. Wang, J. Hu, *ACS Nano* **2011**, *5*, 9761 – 9771; d) K. Yang, S. Zhang, G. Zhang, X. Sun, S.-T. Lee, Z. Liu, *Nano Lett.* **2010**, *10*, 3318 – 3323; e) K. Yang, L. Hu, X. Ma, S. Ye, L. Cheng, X. Shi, C. Li, Y. Li, Z. Liu, *Adv. Mater.* **2012**, *24*, 1868 – 1872; f) Y. Wang, K. C. Black, H. Luehmann, W. Li, Y. Zhang, X. Cai, D. Wan, S.-Y. Liu, M. Li, P. Kim, *ACS Nano* **2013**, *7*, 2068 – 2077; g) Z. Zhang, J. Wang, C. Chen, *Adv. Mater.* **2013**, *25*, 3869 – 3880; h) Y. Liu, K. Ai, J. Liu, M. Deng, Y. He, L. Lu, *Adv. Mater.* **2012**, *24*, 1353 – 1359; i) L. Cheng, K. Yang, Q. Chen, Z. Liu, *ACS Nano* **2012**, *6*, 5605 – 5613; j) G. Shan, R. Weissleder, S. A. Hilderbrand, *Theranostics* **2013**, *3*, 267 – 274.

[3] K. Yang, H. Xu, L. Cheng, C. Sun, J. Wang, Z. Liu, *Adv. Mater.* **2012**, *24*, 5586 – 5592.

[4] a) L. Cheng, K. Yang, Y. Li, J. Chen, C. Wang, M. Shao, S.-T. Lee, Z. Liu, *Angew. Chem.* **2011**, *123*, 7523 – 7528; *Angew. Chem. Int. Ed.* **2011**, *50*, 7385 – 7390; b) Z. Zha, Z. Deng, Y. Li, C. Li, J. Wang, S. Wang, E. Qu, Z. Dai, *Nanoscale* **2013**, *5*, 4462 – 4467; c) Q. Tian, J. Hu, Y. Zhu, R. Zou, Z. Chen, S. Yang, R.-W. Li, Q. Su, Y. Han, X. Liu, *J. Am. Chem. Soc.* **2013**, *135*, 8571 – 8577; d) R. Xiong, S. J. Soenen, K. Braeckmans, A. G. Skirtach, *Theranostics* **2013**, *3*, 141 – 151; e) P. Huang, Z. Li, J. Lin, D. Yang, G. Gao, C. Xu, L. Bao, C. Zhang, K. Wang, H. Song, H. Hu, D. Cui, *Biomaterials*, **2011**, *32*, 3447 – 3458.

[5] a) S. Lal, S. E. Clare, N. J. Halas, *Acc. Chem. Res.* **2008**, *41*, 1842 – 1851; b) X. Huang, P. K. Jain, I. H. El-Sayed, M. A. El-Sayed, *Nanomedicine* **2007**, *2*, 681 – 693; c) Z. Li, P. Huang, X. Zhang, J. Lin, S. Yang, B. Liu, F. Gao, P. Xi, Q. Ren, D. Cui, *Mol. Pharm.* **2009**, *7*, 94 – 104; d) P. Huang, O. Pandoli, X. Wang, Z. Wang, Z. Li, C. Zhang, F. Chen, J. Lin, D. Cui, X. Chen, *Nano Res.* **2012**, *5*, 630 – 639; e) Z. Zhang, J. Wang, C. Chen, *Theranostics* **2013**, *3*, 223 – 238; f) E. Y. Lukianova-Hleb, X. Ren, D. Townley, X. Wu, M. E. Kupferman, D. O. Lapotko, *Theranostics* **2012**, *2*, 976 – 987.

[6] S. C. Gad, K. L. Sharp, C. Montgomery, J. D. Payne, G. P. Goodrich, *Int. J. Toxicol.* **2012**, *31*, 584 – 594.

[7] N. Khlebtsov, V. Bogatyrev, L. Dykman, B. Khlebtsov, S. Staroverov, A. Shirokov, L. Matora, V. Khanadeev, T. Pylaev, N. Tsyganova, *Theranostics* **2013**, *3*, 167 – 180.

[8] a) J. Lin, S. Wang, P. Huang, Z. Wang, S. Chen, G. Niu, W. Li, J. He, D. Cui, G. Lu, *ACS Nano* **2013**, *7*, 5320 – 5329; b) J. He, X. Huang, Y.-C. Li, Y. Liu, T. Babu, M. A. Aronova, S. Wang, Z. Lu, X. Chen, Z. Nie, *J. Am. Chem. Soc.* **2013**, *135*, 7974 – 7984.

[9] J. He, Y. Liu, T. Babu, Z. Wei, Z. Nie, *J. Am. Chem. Soc.* **2012**, *134*, 11342 – 11345.

[10] B. Gao, M. Rozin, A. R. Tao, *Nanoscale* **2013**, *5*, 5677 – 5691.

[11] C. M. Hessel, V. P. Pattani, M. Rasch, M. G. Panthani, B. Koo, J. W. Tunnell, B. A. Korgel, *Nano Lett.* **2011**, *11*, 2560 – 2566.

[12] F. Gassner, A. Owen, *Polymer* **1994**, *35*, 2233 – 2236.

[13] a) P. Huang, C. Xu, J. Lin, C. Wang, X. Wang, C. Zhang, X. Zhou, S. Guo, D. Cui, *Theranostics* **2011**, *1*, 240 – 250; b) M. He, P. Huang, C. Zhang, H. Hu, C. Bao, G. Gao, R. He, D. Cui, *Adv. Funct. Mater.* **2011**, *21*, 4470 – 4477.

[14] a) A. Albanese, P. S. Tang, W. C. W. Chan, *Annu. Rev. Biomed. Eng.* **2012**, *14*, 1 – 16; b) W. H. De Jong, W. I. Hagens, P. Krystek, M. C. Burger, A. J. A. M. Sips, R. E. Geertsma, *Biomaterials* **2008**, *29*, 1912 – 1919; c) S. M. Moghimi, A. C. Hunter, J. C. Murray, *FASEB J.* **2005**, *19*, 311 – 330.

[15] X. Huang, X. Peng, Y. Wang, Y. Wang, D. M. Shin, M. A. El-Sayed, S. Nie, *ACS Nano* **2010**, *4*, 5887 – 5896.